


Macroscopic electric polarization and microscopic electron dynamics: Quantitative insight from femtosecond x-ray diffraction

Christoph Hauf,^{*} Michael Woerner,[†] and Thomas Elsaesser

Max-Born-Institut für Nichtlineare Optik und Kurzzeitspektroskopie, 12489 Berlin, Germany

 (Received 2 May 2018; revised manuscript received 13 July 2018; published 24 August 2018)

The link between macroscopic electric polarizations and microscopic charge densities, a fundamental problem of condensed matter physics, has been addressed by quantum theory involving geometric quantum phases for calculating polarization differences. While such work has provided quantitative insight into stationary electric polarizations of crystalline ferroelectrics, polarization dynamics driven by elementary electronic and/or lattice excitations are still far from understood. X-ray diffraction with a femtosecond time resolution allows for mapping of charge and lattice motions on their intrinsic time scales and provides time-dependent maps of electron density. We present a combined theoretical and experimental approach which allows for determining time-dependent macroscopic polarization changes from transient microscopic charge density maps. In an extension of existing theory, the key steps consist of deriving a microscopic current density from the charge density maps and calculating the macroscopic polarization change from this current density. Using femtosecond x-ray diffraction data for crystalline $(\text{NH}_4)_2\text{SO}_4$ and KH_2PO_4 , prototype materials displaying ferro- and paraelectric phases, we determine the ultrafast macroscopic polarization dynamics induced by coherent phonon motions. The results establish femtosecond x-ray diffraction as a key method for grasping transient polarization changes and for validating theoretical predictions for a wide range of polar and ferroelectric materials.

DOI: [10.1103/PhysRevB.98.054306](https://doi.org/10.1103/PhysRevB.98.054306)

I. INTRODUCTION

Electric polarization, a macroscopic quantity of classical electrodynamics, describes a wide range of stationary and transient electric phenomena in condensed matter. In polar or ionic materials, e.g., ferroelectrics, a spatial charge separation at the atomic level gives rise to spontaneous polarization [1,2]. The application of external electric fields can induce time-dependent polarizations which are described with the help of linear and/or nonlinear susceptibilities. This concept has been applied widely in linear and nonlinear optics [3] and for addressing optically induced charge transport [4].

The definition of macroscopic polarizations in terms of microscopic electric quantities such as electronic and nuclear charge densities, dipole moments, and currents has remained a challenging problem, requiring a link between quantum and macroscopic physics. Extensive theoretical work has shown that simplistic concepts relating stationary microscopic charge densities $\rho_0(\mathbf{r})$ to the macroscopic polarization are ill defined and lead to ambiguous results, except for cases in which electronic charge is entirely localized, e.g., on ionic sites [5,6]. In general, only polarization *differences* between different states of a system are well defined, a fact that has direct consequences for a proper theoretical description. In their pioneering analysis, Resta, Vanderbilt, and others have presented a quantum mechanical concept, the geometric phase approach, for calculating macroscopic polarization differences between different states of a solid from differential microscopic

charge densities which have been cast as quantum currents [6–9]. The currents are related to quantum phases, which in crystals are calculated from the cell-periodic part of the electronic wave function.

The geometric phase approach focuses on the electronic contribution to the polarization difference, which is determined by calculating the geometrical (Berry) phase change along an adiabatic quantum path between the two states. As shown in Ref. [10], the application of Stokes' theorem allows for calculation of the final state of the quantum-mechanical adiabatic motion without knowledge of the spatiotemporal phase of the wave function along the adiabatic path. A closer inspection shows [cf. Eq. (3) in Ref. [10]] that the procedure does not fulfill the continuity equation for electric charge because even though electronic charge is moved in real space, the expectation value of the current density operator $\langle \mathbf{j}(\mathbf{r}, t) \rangle = 0$ vanishes at all times, due to the adiabatic character of the charge motion [11,12]. While this treatment is fully appropriate for calculating differences of stationary macroscopic polarizations, it cannot account for time-dependent macroscopic polarization differences which originate from real transient microscopic currents.

There are numerous cases in which macroscopic polarizations change as a consequence of changes imposed on microscopic structure, i.e., atomic displacements and electronic charge. Phase transitions between para- and ferroelectric crystalline structures have been rationalized by both order-disorder transitions in a crystal structure [13] and the fundamental soft-mode concept [14,15]. The excitation of a particular phonon, the soft mode, is connected with subpicometer atomic displacements which induce a spatial relocation of electronic charge over much larger distances in the 100-pm range. This

^{*}hauf@mbi-berlin.de

[†]woerner@mbi-berlin.de

behavior originates from the subtle interplay of valence and electric forces in a polar crystal lattice, which makes the spatial distribution of valence electronic charge most sensitive to small changes in the atomic arrangement.

Recently, such behavior has been validated by experiments in which a number of polar materials were studied under nonequilibrium conditions by ultrafast x-ray diffraction [16–21]. Here, excitation of lattice vibrations with a period in the femtosecond to few picosecond range induces pronounced charge relocations on the 100-pm length scale of chemical bonds. Transient charge density maps derived from the femtosecond x-ray diffraction data have allowed for following such dynamics in a spatially and time-resolved way.

Polarization changes induced by time-dependent elementary excitations call for an extension of the existing theoretical framework in order to link transient macroscopic polarization changes to charge dynamics at the microscopic level. In this article, we present a theoretical approach which allows for determination of macroscopic polarization changes from time-dependent microscopic charge density maps. To illustrate the potential of the method, we analyze femtosecond x-ray diffraction data for $(\text{NH}_4)_2\text{SO}_4$ (AS) and KH_2PO_4 (KDP), both being prototype materials with different para- and ferroelectric phases. Building upon the extensive results of femtosecond x-ray diffraction experiments presented in Refs. [19–21], we here extend the analysis of transient electron density distributions in AS and KDP to derive time-dependent microscopic current densities and macroscopic polarization changes.

The article is organized as follows. In Sec. II, we discuss the theoretical concept for linking microscopic time-dependent charge densities to macroscopic polarization changes. The first application of the method to AS is presented in Sec. III. The model system KDP is discussed in Sec. IV, including a symmetry analysis of phonon excitations in the para- and ferroelectric phases, transient charge density maps, and the resulting macroscopic polarizations. Conclusions and an outlook are presented in Sec. V.

II. THEORETICAL CONCEPTS

A. Electric polarization in condensed matter

Microscopic electric polarizations $\mathbf{P}(\mathbf{r}, t)$ and/or magnetizations $\mathbf{M}(\mathbf{r}, t)$, i.e., dipole densities, are *not* uniquely defined physical quantities and, thus, cannot be measured directly in any experiment. It was shown in Ref. [22] that the microscopic $\mathbf{P}(\mathbf{r}, t)$ and $\mathbf{M}(\mathbf{r}, t)$ are not defined uniquely, similar to the well-known ambiguity of the scalar $V(\mathbf{r}, t)$ and vector $\mathbf{A}(\mathbf{r}, t)$ potential fields which determine the measurable electric $\mathbf{E}(\mathbf{r}, t)$ and magnetic $\mathbf{B}(\mathbf{r}, t)$ fields. This fact is evident from the Maxwell equations in matter:

$$\nabla \cdot \mathbf{B}(\mathbf{r}, t) = 0, \quad (1)$$

$$\begin{aligned} \varepsilon_0 \nabla \cdot \mathbf{E}(\mathbf{r}, t) &= \rho(\mathbf{r}, t) \\ &= -\nabla \cdot [\mathbf{P}(\mathbf{r}, t) + \nabla \times \mathbf{C}(\mathbf{r}, t)], \end{aligned} \quad (2)$$

$$\nabla \times \mathbf{E}(\mathbf{r}, t) = -\frac{\partial \mathbf{B}(\mathbf{r}, t)}{\partial t}, \quad (3)$$

$$\begin{aligned} \frac{1}{\mu_0} \nabla \times \mathbf{B}(\mathbf{r}, t) &= \varepsilon_0 \frac{\partial \mathbf{E}(\mathbf{r}, t)}{\partial t} + \mathbf{j}(\mathbf{r}, t) \\ &= \varepsilon_0 \frac{\partial \mathbf{E}(\mathbf{r}, t)}{\partial t} + \frac{\partial}{\partial t} [\mathbf{P}(\mathbf{r}, t) + \nabla \times \mathbf{C}(\mathbf{r}, t)] \\ &\quad + \nabla \times \left[\mathbf{M}(\mathbf{r}, t) - \frac{\partial}{\partial t} \mathbf{C}(\mathbf{r}, t) \right]. \end{aligned} \quad (4)$$

In the Maxwell equations containing, on the right-hand side, the (measurable) charge density $\rho(\mathbf{r}, t)$ [Eq. (2)] and current density $\mathbf{j}(\mathbf{r}, t)$ [Eq. (4)], the terms in the brackets represent the most general definition of $\mathbf{P}(\mathbf{r}, t)$ and $\mathbf{M}(\mathbf{r}, t)$, which contain the arbitrary (differentiable) vector field $\mathbf{C}(\mathbf{r}, t)$. As mentioned explicitly in Eqs. (2-9a) and (2-9b) in Ref. [22], all definitions of $\mathbf{P}(\mathbf{r}, t)' = \mathbf{P}(\mathbf{r}, t) + \nabla \times \mathbf{C}(\mathbf{r}, t)$ and $\mathbf{M}(\mathbf{r}, t)' = \mathbf{M}(\mathbf{r}, t) - \frac{\partial}{\partial t} \mathbf{C}(\mathbf{r}, t)$ are equally acceptable. $\mathbf{P}_t(\mathbf{r}, t)$, the transverse component of the electric polarization $\mathbf{P}(\mathbf{r}, t)$, is then characterized by a vanishing divergence $\nabla \cdot \mathbf{P}_t(\mathbf{r}, t) = 0$. Thus $\mathbf{P}_t(\mathbf{r}, t)$ can be arbitrarily modified without violating the continuity equation of electric charge or modifying any of the directly measurable physical quantities $\mathbf{E}(\mathbf{r}, t)$, $\mathbf{B}(\mathbf{r}, t)$, $\rho(\mathbf{r}, t)$, and $\mathbf{j}(\mathbf{r}, t)$.

A popular approach in theoretical nonlinear optics and the theory of ferroelectrics has consisted of using microscopic and macroscopic electric polarizations in parallel. This means that in crystalline solids one typically averages the electric dipole moment over the unit cell of the crystal to determine the macroscopic polarization. This method is ill defined as pointed out in Refs. [5] and [6]. For nonmagnetic insulators one can always choose a vector field $\mathbf{C}(\mathbf{r}, t)$ to get $\mathbf{M}(\mathbf{r}, t) = 0$ in Eqs. (2) and (4). In doing so, one can add to $\mathbf{P}(\mathbf{r}, t)$ an arbitrary homogeneous vector field without violating the Maxwell equations and continuity equation for electric charge. Thus, there are no absolute microscopic and macroscopic electric polarizations which could be determined in an experiment. Moreover, there is no *direct* link between the time-dependent change of the charge density $\Delta\rho(\mathbf{r}, t)$ and the change of the macroscopic electric polarization $\Delta\mathbf{P}(\mathbf{r}, t)$ in periodic solids [23]. A way out of this dilemma is to take the microscopic current density as the basic physical quantity $\mathbf{j}(\mathbf{r}, t)$ and to define the polarization change between time t_1 and time t_2 via

$$\Delta\mathbf{P}(\mathbf{r}, t_1, t_2) = \mathbf{P}(\mathbf{r}, t_2) - \mathbf{P}(\mathbf{r}, t_1) = \int_{t_1}^{t_2} \mathbf{j}(\mathbf{r}, t) dt. \quad (5)$$

Macroscopic polarizations are determined by averaging microscopic polarizations over a certain integration volume. In crystalline materials with periodic charge and current densities the macroscopic polarization is identical in each unit cell and, thus, loses its spatial dependence. We, thus, define the macroscopic polarization change as

$$\Delta\mathbf{P}^{\text{UC}}(t_1, t_2) = \frac{1}{V_{\text{uc}}} \int_{\text{unit cell}} d^3\mathbf{r} \Delta\mathbf{P}(\mathbf{r}, t_1, t_2). \quad (6)$$

where V_{uc} is the volume of the unit cell. The symmetry of the unit cell of a crystal represents a basic constraint to be fulfilled by the microscopic current density. Obviously, for unit cells containing current densities $\mathbf{j}(\mathbf{r}, t)$ whose projections on particular axes [e.g., $J_z(z, t) = \int_0^a dx \int_0^b dy \mathbf{j}(\mathbf{r}, t) \dots$, etc.] contain inversion centers, the macroscopic current identically vanishes,

$\mathbf{J}(t) = \int_0^a dx \int_0^b dy \int_0^c dz \mathbf{j}(\mathbf{r}, t) = 0$, as, consequently, does the change of macroscopic polarization $\Delta \mathbf{P}^{\text{UC}} = 0$.

B. Microscopic currents and transient charge densities

We present a theoretical method which allows for the reconstruction of $\Delta \mathbf{P}(\mathbf{r}, t)$ from the time-dependent change of the charge density $\rho(\mathbf{r}, t)$, a quantity which is directly accessible by time-resolved x-ray diffraction experiments. The charge density is connected to the microscopic current density $\mathbf{j}(\mathbf{r}, t)$ via the continuity equation of electronic charge:

$$\begin{aligned} \frac{\partial \rho(\mathbf{r}, t)}{\partial t} &= \dot{\rho}(\mathbf{r}, t) \\ &= -\nabla \cdot \mathbf{j}(\mathbf{r}, t) = -\nabla \cdot [\rho(\mathbf{r}, t) \mathbf{v}(\mathbf{r}, t)]. \end{aligned} \quad (7)$$

Similarly to the relation between $\rho(\mathbf{r}, t)$ and the microscopic polarization $\mathbf{P}(\mathbf{r}, t)$ in Eq. (2), there is no unique relation between $\mathbf{j}(\mathbf{r}, t)$ and the temporal change of the charge density $\dot{\rho}(\mathbf{r}, t)$. A straightforward integration of Eq. (7) gives

$$\begin{aligned} \mathbf{j}(\mathbf{r}, t) &= -\frac{\hat{\mathbf{e}}_x}{3} \int_0^x ds \dot{\rho}(s, y, z, t) - \frac{\hat{\mathbf{e}}_y}{3} \int_0^y ds \dot{\rho}(x, s, z, t) \\ &\quad - \frac{\hat{\mathbf{e}}_z}{3} \int_0^z ds \dot{\rho}(x, y, s, t) + \nabla \times \mathbf{U}(\mathbf{r}, t), \end{aligned} \quad (8)$$

with the unit vectors $\hat{\mathbf{e}}_x$, $\hat{\mathbf{e}}_y$, and $\hat{\mathbf{e}}_z$ in the spatial directions x , y , and z defining a Cartesian coordinate system. Because Eq. (8) contains the arbitrary (differentiable) vector field $\mathbf{U}(\mathbf{r}, t)$, the transverse component of, and consequently its spatially homogeneous contribution to, the microscopic current density $\mathbf{j}(\mathbf{r}, t)$ can be arbitrarily modified without violating the continuity equation, (7). Thus, an additional constraint is required for determining the current density vector field $\mathbf{j}(\mathbf{r}, t)$ uniquely. To this end, we assume that the entire electron ensemble performs a quasiadiabatic motion, i.e., the wave function of the electronic system stays at all times as close as possible to a certain stationary eigenstate of the electronic Hamiltonian. In Appendix A we briefly discuss a ‘‘hydrodynamical’’ formulation of quantum mechanics which explicitly shows that the quasiadiabatic motion of electrons corresponds to the velocity field $\mathbf{v}(\mathbf{r}, t) = \mathbf{j}(\mathbf{r}, t)/\rho(\mathbf{r}, t)$, which contains the lowest additional kinetic energy of the electrons,

$$\begin{aligned} W_{\text{kin}}(t) &= \frac{m_e}{2(-e_0)} \int dV \rho(\mathbf{r}, t) |\mathbf{v}(\mathbf{r}, t)|^2 \\ &= \frac{m_e}{2(-e_0)} \int dV \frac{|\mathbf{j}(\mathbf{r}, t)|^2}{\rho(\mathbf{r}, t)}, \end{aligned} \quad (9)$$

relative to the energy of the stationary eigenstate of the electronic Hamiltonian in which the quasiadiabatic motion is performed. In the following we search for the three-dimensional current density $\mathbf{j}(\mathbf{r}, t)$ which fulfills the continuity equation, (7), and minimizes the kinetic energy of the electrons [Eq. (9)] during their motion. The concrete numerical procedure is described in Appendix B.

C. Reconstruction of transient charge densities from x-ray diffraction experiments

X-ray diffraction from single crystals or crystalline powders represents a key method for determining spatially resolved

equilibrium electron densities in crystalline matter. An analysis of the x-ray intensity diffracted from the set of lattice planes (hkl) provides the modulus of the respective structure factor F_{hkl}^0 , a complex quantity given by the (spatial) Fourier transform of the electron density. Different approaches such as multipole refinements and the maximum entropy method (MEM) have allowed for deriving highly accurate stationary electron densities $\rho_0(\mathbf{r})$ from diffraction patterns with a high number of diffraction peaks or Debye-Scherrer rings [24,25]. The advent of femtosecond laser-driven and accelerator-based hard x-ray sources has paved the way towards ultrafast x-ray diffraction which allows for mapping of atomic motions and charge relocations on their intrinsic time scales. Most experiments have applied pump-probe schemes in which an optical pump pulse initiates a structure change, which is followed by diffraction of a delayed hard x-ray probe pulse from the excited sample. A measurement of diffraction patterns for different pump-probe delays then maps the time evolution of the structure changes.

In a series of studies we have shown that femtosecond x-ray powder diffraction represents an attractive and versatile tool for reconstructing *transient*, i.e., *time-dependent* electron densities from patterns of Debye-Scherrer rings [17–21,26]. Time-resolved powder diffraction data allow for derivation of transient difference density maps $\Delta \rho(\mathbf{r}, t) = \rho(\mathbf{r}, t) - \rho_0(\mathbf{r})$ if the following conditions are fulfilled: (i) the initial electron density $\rho_0(\mathbf{r})$ is known with a high accuracy from stationary x-ray crystallography, and (ii) the transient modification of the ensemble-averaged charge density is at all times small compared to that of the initial structure $|\Delta \rho(\mathbf{r}, t)| \ll \rho_0(\mathbf{r})$. Since the structure factors $F_{hkl}(t)$ are the three-dimensional Fourier transform of the spatially periodic electron density $\rho(\mathbf{r}, t)$, the latter condition corresponds to $|\Delta F_{hkl}| \ll |F_{hkl}^0|$. An appropriate tool for reconstructing the transient difference density map $\Delta \rho(\mathbf{r}, t)$ from the relative changes of the diffracted x-ray intensity $[I_{hkl}(t) - I_{hkl}^0]/I_{hkl}^0 = [|F_{hkl}(t)|^2 - |F_{hkl}^0|^2]/|F_{hkl}^0|^2$ is the MEM [27], which fully exploits all information from the known initial structure. $\Delta \rho(\mathbf{r}, t)$ is then reconstructed on a three-dimensional grid with a typical grid spacing of 0.1 Å. We have described the application of the MEM to femtosecond powder diffraction data in detail in Ref. [28].

The transient powder diffraction patterns are averaged over the random spatial orientation of crystallites in the powder. As a result, the differential charge density map $\Delta \rho_{\text{ave}}(\mathbf{r}, t)$ is averaged over all manifestations of the transient structure changes, i.e., the electron density reconstructed from the (symmetry-allowed) x-ray diffraction rings possesses a symmetry identical to that of the initial structure $\rho_0(\mathbf{r})$. A break of this symmetry would lead to the occurrence of new, initially forbidden peaks in the transient diffraction patterns. In most studies performed so far, forbidden peaks have not been observed or have been of minor relevance [18].

III. MICROSCOPIC CURRENTS AND MACROSCOPIC POLARIZATION DYNAMICS IN FERROELECTRIC AMMONIUM SULFATE [(NH₄)₂SO₄]

Crystalline ammonium sulfate is a prototype ionic material which displays a macroscopic ferroelectric polarization below

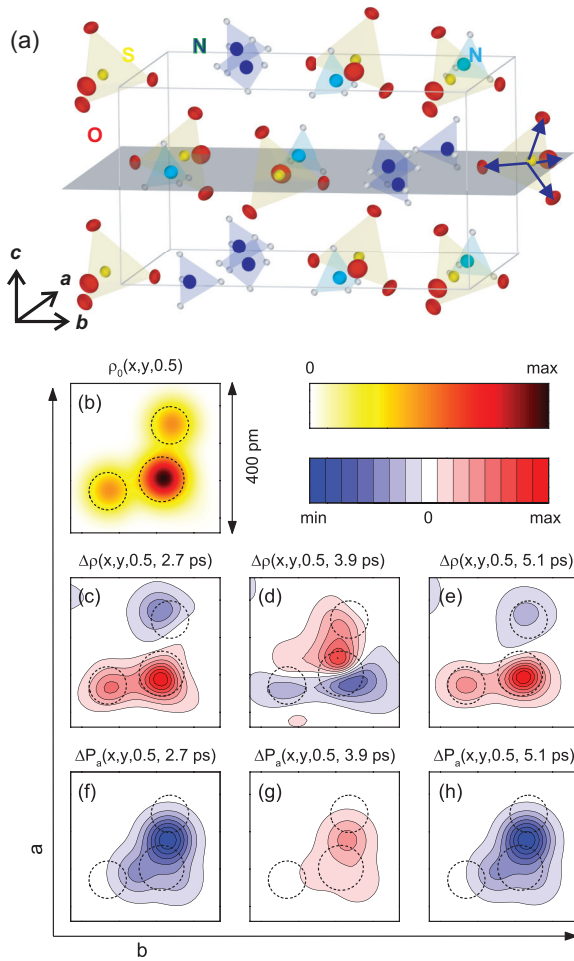


FIG. 1. (a) Crystal lattice of ferroelectric ammonium sulfate $[(\text{NH}_4)_2\text{SO}_4]$ with tilted ammonium (NH_4^+) tetrahedra (nitrogen, blue; hydrogen, white) and sulfate (SO_4^{2-}) tetrahedra (sulfur, yellow; oxygen, red). Blue arrows: local dipoles between sulfur and oxygen atoms. (b) Stationary electron density map $\rho_0(x, y, z = 0.5)$ in the gray plane around the sulfate ion with blue arrows, displaying high values on the sulfur (red) and lower values on the oxygens (yellow) with $\rho_0^{\min} = 0$ and $\rho_0^{\max} = 12\,000\ e^-/\text{nm}^3$. (c–e) Difference density maps $\Delta\rho(x, y, 0.5, t)$ for delay times of $t = 2.7\ \text{ps}$, $t = 3.9\ \text{ps}$, and $t = 5.1\ \text{ps}$ with $\Delta\rho_0^{\min} = -75\ e^-/\text{nm}^3$ and $\Delta\rho_0^{\max} = +75\ e^-/\text{nm}^3$. (f–h) Calculated microscopic polarization changes along the a axis $\Delta P_a(x, y, 0.5, t) = \int_{-\infty}^t j_x(x, y, 0.5, s) ds$ assuming quasiadiabatic motions of the electrons for the same delay times with $\Delta P_a^{\min} = -1\ \text{C/m}^2$ and $\Delta P_a^{\max} = +1\ \text{C/m}^2$.

the transition temperature $T_C = 223\ \text{K}$ [29]. In Fig. 1(a) we show the crystal structure of ferroelectric AS, which consists of tilted ammonium (NH_4^+) and sulfate (SO_4^{2-}) tetrahedra and belongs to the orthorhombic space group $Pna2_1$ [No. 33 in the International Tables for Crystallography (ITA)], point group ($mm2$), with the polar axis parallel to the crystallographic c axis. The blue arrows in the sulfate ion on the right-hand side indicate local dipoles between sulfur and oxygen atoms. The stationary electron density $\rho_0(\mathbf{r})$ of ferroelectric AS was derived from stationary x-ray diffraction experiments with single crystals [21,30]. In Fig. 1(b), a sectional view of the electron density $\rho_0(x, y, z = 0.5)$ [gray plane in Fig. 1(a)] is

shown in a subvolume around the sulfate ion with the blue arrows. The electron density is highest on the sulfur atom and lower on the two oxygens.

Charge dynamics in this system has recently been studied in femtosecond x-ray diffraction experiments with powders of small AS crystallites in the ferroelectric phase at a temperature of $T = 200\ \text{K}$ [21]. An optical pump pulse with a center wavelength of $400\ \text{nm}$ induces coherent vibrational motions of the crystal lattice, and a delayed hard x-ray probe pulse scattered from the excited sample generates momentary Debye-Scherrer diffraction patterns. Additional experimental details are given in Ref. [21]. Transient differential charge density maps $\Delta\rho(\mathbf{r}, t) = \rho(\mathbf{r}, t) - \rho_0(\mathbf{r})$ were derived from the diffraction data with the help of the MEM on a $72 \times 108 \times 64$ grid. The coherent lattice motions, which are dominated by a low-frequency mode with a 2.7-ps period (frequency, $0.36\ \text{THz}$), cause a significant oscillatory charge transfer within the sulfate ions, the strongest of which is shown in the $\Delta\rho(x, y, 0.5, t)$ maps in Figs. 1(c)–1(e) for delay times of $t = 2.7\ \text{ps}$, $t = 3.9\ \text{ps}$, and $t = 5.1\ \text{ps}$. As discussed in detail in Ref. [21], the distances over which electronic charge is shifted are 3 orders of magnitude larger than the atomic displacements connected with the 0.36-THz mode, suggesting a soft-mode character of the latter. Due to the known phenomenon of inhomogeneous broadening of the frequencies of infrared-active phonons, these oscillations are severely damped on a time scale of several picoseconds in our powder samples [21].

For a reconstruction of the macroscopic polarization change $\Delta\mathbf{P}^{\text{UC}}(t)$, i.e., the microscopic polarization $\Delta\mathbf{P}(\mathbf{r}, t)$ averaged over the unit cell of ferroelectric AS, it is sufficient to solve the continuity equation, (7), using the time-dependent $\Delta\rho_{\text{ave}}(\mathbf{r}, t)$ of the unit cell averaged over all orientations in the powder. This simplified treatment is sufficient because ferroelectric AS consists of neutral molecular arrangements in layers parallel to the ab plane of its unit cell. Such layers are separated by regions of extremely low electron density. Microscopic currents flowing between neighboring molecular layers are negligible, even for lattice oscillations with a symmetry belonging to IRREP A_1 , the irreducible representation of the point group ($mm2$) which possesses the full symmetry of the ferroelectric unit cell. In the language of Resta this behavior corresponds to the ‘‘Clausius-Mossotti’’ case [6]. To solve Eq. (7), one can choose the (uneven) interface of lowest electron density as a boundary between two adjacent subvolumes in the c direction, over which the averaging of the electric field (created by electronic charge) is then performed to calculate the electronic contribution to the macroscopic $\Delta\mathbf{P}^{\text{UC}}(t)$ [21]. The main contribution to $\Delta\mathbf{P}^{\text{UC}}(t)$ is due to the anisotropic transfer of electronic charge within the sulfate ions [cf. Figs. 1(c)–1(e)].

We now go one step further and address the dynamics of local dipole changes $\Delta\mathbf{d}$ in the sulfate ions [sketched as blue arrows in Fig. 1(a)] for which the knowledge of the microscopic current density $\mathbf{j}(\mathbf{r}, t)$ is relevant. Following the theoretical approach in Sec. II B, the coupled equations, (7) and (9), are solved to determine $\mathbf{j}(\mathbf{r}, t)$ from the charge density $\rho(\mathbf{r}, t)$ as derived from the diffraction experiment. The microscopic polarization changes along the a axis $\Delta P_a(x, y, 0.5, t) = \int_{-\infty}^t j_x(x, y, 0.5, s) ds$, which are shown for the different delay times in Figs. 1(f) to 1(h). The highest microscopic polarization

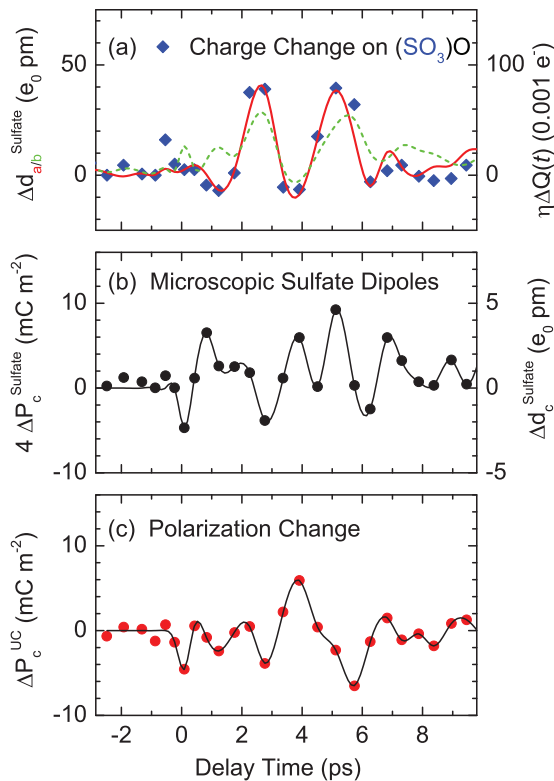


FIG. 2. (a) Diamonds: Transient charge change of the SO_3 subgroup within the sulfate ion (identical to Fig. 5(b) in Ref. [21]). The dipole change $\Delta d_a(t)$ along the a axis (solid red line) of a single sulfate ion follows almost perfectly the electronic charge transfer from the upper oxygen atom to the SO_3 subgroup, obvious in Figs. 1(c) to 1(e). The dipole change $\Delta d_b(t)$ along the b axis (dashed green line) is somewhat smaller and shows additional contributions. (b) The dipole change $\Delta d_c(t)$ (right vertical axis) along the c axis (solid black line) of a single sulfate ion is an order of magnitude smaller and shows a temporal behavior quite different from those along the a and b axes. The corresponding macroscopic polarization of all four sulfate ions belonging to a single unit cell (left vertical axis) is very similar to that of the entire unit cell shown in (c) (cf. Fig. 8(c) in Ref. [21]).

changes occur exactly on the chemical bonds within the sulfate ions, i.e., the spatial regions between the dashed circles indicating the atomic positions. Our theoretical treatment confirms this intuitive physical picture and, at the same time, allows for a quantitative analysis of microscopic polarization changes along various spatial directions, among them the change along the a axis $\Delta P_a(x, y, 0.5, t) = \int_{-\infty}^t j_x(x, y, 0.5, s) ds$.

In Fig. 2(a) the diamonds represent the transient charge change of the SO_3 subgroup within the sulfate ion (right ordinate scale; cf. Fig. 5(b) in Ref. [21]). Integrating the microscopic current density $\mathbf{j}(\mathbf{r}, t)$ over time and the subvolume of a single sulfate ion allows for calculation of transient dipole changes along various axes. The dipole change $\Delta d_a(t)$ along the a axis of a single sulfate ion is plotted as the solid red line in Fig. 2(a). Its transient follows almost perfectly the electronic charge transfer from the upper oxygen atom to the SO_3 subgroup (blue diamonds). The dipole change $\Delta d_b(t)$ along the b axis, shown as the dashed green line, is somewhat smaller and shows additional contributions. We would like

to stress the fact that although individual sulfate ions show large transient dipoles along the a and b directions, they do not create macroscopic polarizations along those directions because for symmetry reasons the unit cell contains another sulfate ion with opposite dipole moments in the a and b directions.

The dipole change $\Delta d_c(t)$ [right vertical axis in Fig. 2(b)] along the c axis [solid black line in Fig. 2(b)] of a single sulfate ion is an order of magnitude smaller and shows a temporal behavior quite different from those along the a and b axes. In addition, all transient dipoles of sulfate ions within the unit cell of AS point in the same direction and give the dominant contribution to the macroscopic polarization $\Delta P_c^{\text{UC}}(t)$ of the crystal, which is given by the spatial average of $\Delta P_c(\mathbf{r}, t)$ over the unit cell. The left axis in Fig. 2(b) shows the corresponding macroscopic polarization of all four sulfate ions belonging to a single unit cell. A comparison with the total macroscopic polarization along the c axis [Fig. 2(c)] which includes contributions from the NH_4^+ units shows a very similar temporal behavior and demonstrates the dominance of intramolecular electronic dipoles within the sulfate ions to the soft-mode polarization in ferroelectric AS.

IV. STRUCTURAL DYNAMICS IN THE PARAELECTRIC PHASE OF KH_2PO_4

KDP represents a ferroelectric with a lattice structure that is determined by Coulomb interactions between the ionic subunits K^+ and H_2PO_4^- and by hydrogen bonds between adjacent H_2PO_4^- groups [31]. At $T = 300$ K, KDP crystallizes in the tetragonal space group $I\bar{4}2d$ ($a = 0.74521$ nm, $c = 0.69740$ nm) with four formula units in the unit cell [Fig. 3(a)]. There is no polar axis in this noncentrosymmetric space group, and thus, the material is paraelectric. At the critical temperature $T_c = 123$ K, KDP undergoes a structural phase transition into the nonconventional space group $I21d$, leading to a reduction of the crystal symmetry. In the literature this crystal structure is more commonly reported in the conventional orthorhombic space group $Fdd2$, where the crystallographic a and b axes are rotated by 45° and elongated by a factor of $\sqrt{2}$ ($a = 1.05459$ nm, $b = 1.04664$ nm, $c = 0.69265$ nm) compared to the paraelectric structure [31]. This results in a doubled volume of the unit cell, with eight formula units being present. The change of the atomic arrangement within the H_2PO_4^- ion as well as the displacement of the K^+ ion relative to the phosphorus atom $\Delta R_K(t)$ is illustrated in the inset in Fig. 3(b) and is characterized mainly by a shift of the potassium and oxygen atoms along the c direction. This reduction of symmetry leads to a polar axis in the crystallographic c direction and a ferroelectric polarization along this direction. The absolute value of the spontaneous polarization is $P_s = 47.5$ mC m $^{-2}$ just below $T_c = 123$ K. The microscopic mechanisms of the phase transition have remained controversial [13,32,33].

The interplay of nonequilibrium phonon excitations and spatial relocations of electronic charge in paraelectric KDP has been elucidated in a recent femtosecond x-ray powder diffraction experiment at room temperature. Experimental details and extended data sets have been reported in Refs. [19] and [20]. A stationary powder diffraction pattern obtained in these experiments is presented in Fig. 3(b), including

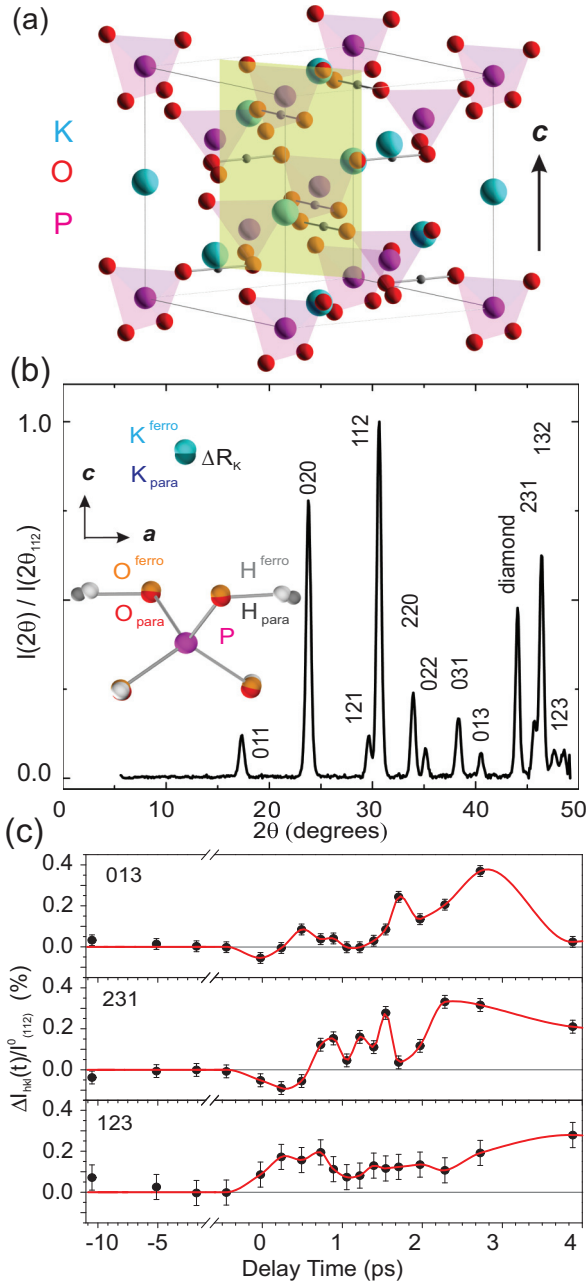


FIG. 3. (a) Equilibrium crystal structure of paraelectric KDP. (b) X-ray powder diffraction pattern of the unexcited paraelectric sample. The normalized diffracted intensity integrated over individual Debye-Scherrer rings is plotted as a function of the scattering angle 2θ , including assignments to lattice planes. Inset: Overlay of the atomic positions of the K^+ and the $H_2PO_4^-$ ions shown by colored spheres in paraelectric and ferroelectric KDP (darker and lighter colors, respectively) to illustrate the structural modifications due to the phase transition. (c) Change of diffracted x-ray intensity upon excitation $\Delta I_{hkl}(t) / I_{hkl}^0$ on three different Bragg reflections as a function of the pump-probe delay in femtosecond experiments at room temperature (black symbols). Red lines are a guide for the eye.

the assignments of the 11 observed Bragg peaks. Optical excitation of KDP by pump pulses with a center wavelength of ≈ 266 nm induces transient changes of the intensities of different Debye-Scherrer rings, as shown in Fig. 3(c), where the

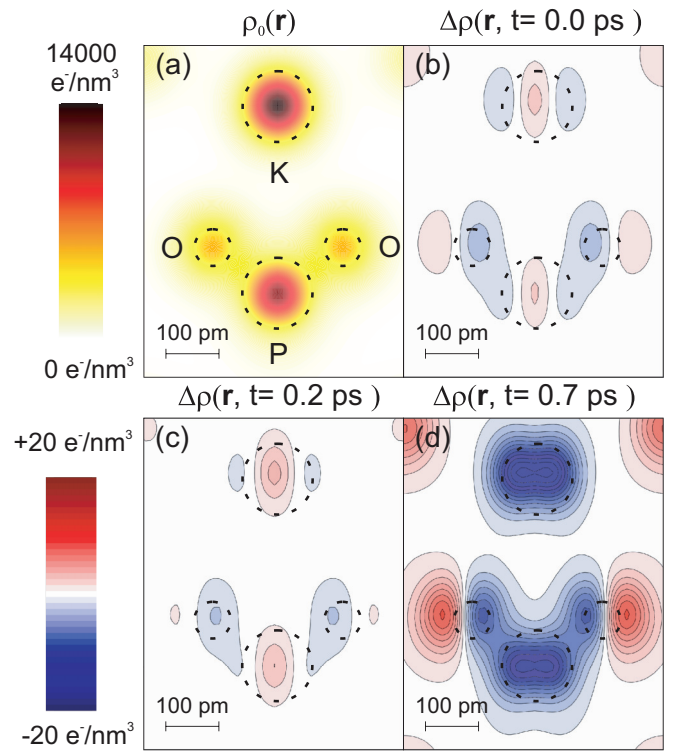


FIG. 4. (a) Equilibrium electron density $\rho_0(\mathbf{r})$ as a two-dimensional contour map in a plane containing a potassium, a phosphorus, and two oxygen atoms [highlighted in yellow in Fig. 3(a)]. (b-d) Transient changes in electron density $\Delta\rho(\mathbf{r}, t)$ with contour intervals of $\pm 1e^-/\text{nm}^3$ in the same plane at selected delay times. The positions of the atoms in the unexcited unit cell are indicated by dashed circles.

relative intensity change $\Delta I_{hkl}(t) / I_{hkl}^0 = (I_{hkl}(t) - I_{hkl}^0) / I_{hkl}^0$ of selected Bragg peaks is plotted as a function of the pump-probe delay [$I_{hkl}(t)$, I_{hkl}^0 : intensity diffracted with and without optical excitation]. A more extensive data set containing a total of 10 transients has been reported in Refs. [19] and [20]. The transient electron density changes $\Delta\rho(\mathbf{r}, t)$ are then derived with the MEM on a $72 \times 72 \times 72$ grid (cf. Sec. II C) taking the full data set into account. This procedure establishes a link between the exact symmetry of the equilibrium electron density $\rho_0(\mathbf{r})$ and the microscopic transient changes in electron density $\Delta\rho(\mathbf{r}, t)$.

Equilibrium and transient charge density maps for different pump-probe delays in a plane containing a potassium, a phosphorus, and two oxygen atoms of the phosphate unit are shown in Fig. 4. The latter reveal a pronounced modulation of charge density with time, close to the original positions of the lattice atoms, which are indicated by dashed circles. In particular, a pronounced oscillatory relocation of electronic charge between the K^+ and the $H_2PO_4^-$ ions as well as within the phosphate unit is observed, in excellent agreement with the results published in Refs. [19] and [20], which were derived with a different method of charge density analysis. The corresponding vibrational elongations at a frequency of around 60 cm^{-1} with an amplitude in the subpicometer range induce charge displacements over distances of the order of 100 pm, i.e., a chemical bond length [19]. This behavior is in line with

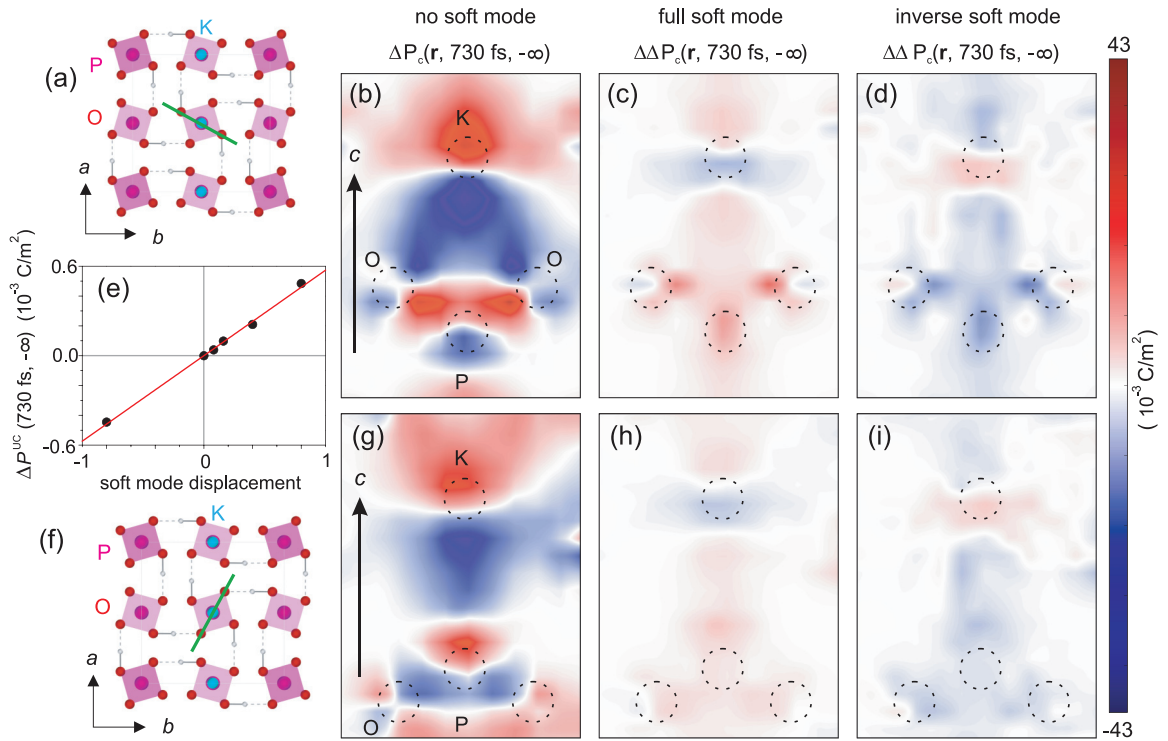


FIG. 5. (a, f) View of the crystal structure of paraelectric KDP along the polar c axis with the two different two-dimensional planes containing a potassium, a phosphor, and two oxygen atoms indicated by green lines. (b, g) Transient changes in the microscopic polarization density $\Delta P(\mathbf{r}, t)$ at a selected delay time ($t \sim 730$ fs) in the planes indicated in (a, f) for a structure in which no additional displacement of the ground-state structure according to the B_2 mode is present. The positions of the atoms in the unexcited unit cell are indicated by dashed circles. The additional changes in the microscopic polarization density $\Delta\Delta P(\mathbf{r}, t)$ at the same delay time caused by a full positive or negative displacement according to the B_2 mode are shown in (c) and (h) and in (d) and (i), respectively. (e) Total change of the macroscopic electric polarization $\Delta P^{\text{UC}}(t)$ at a delay time of $t \sim 730$ fs as a function of the fraction of the full B_2 -mode displacement [37]. The red line represents a linear fit to the data points (black symbols).

the soft-mode character of the TO phonon mode suggested by vibrational spectroscopy [34,35] and the basic physical picture developed in the pioneering work by Cochran [15].

In addition to the soft mode, the analysis of $\Delta\rho(\mathbf{r}, t)$ has also revealed the presence of other phonon modes in photoexcited paraelectric KDP [19,20]. Coherent phonon motions with A_2 , B_1 , or E symmetries would cause a finite intensity of the symmetry-forbidden 110 and 002 reflections, a phenomenon completely absent in our time-resolved experiments [19,20]. Thus, coherent phonons with A_2 , B_1 , or E symmetries can be safely neglected and exclusively coherent phonon motions of A_1 and B_2 symmetry are present. Among them is the soft mode with B_2 character that plays the key role for the polarization dynamics.

The approach, detailed in Sec. II B, now allows for reconstruction of transient changes in the microscopic polarization $\Delta P(\mathbf{r}, t)$ from the $\Delta\rho(\mathbf{r}, t)$ maps. The results are summarized in Fig. 5. It is important to note that the projection of electron density onto the crystallographic (ab) plane perpendicular to the polar c axis of KDP retains inversion symmetry. The oscillatory relocation of the electronic charge is connected with microscopic currents along the a and b directions; the resulting change of macroscopic polarization, however, vanishes due to the crystal symmetry, which is preserved upon excitation in the time-resolved x-ray experiments [19]. Therefore, only microscopic currents along the c direction contribute to a nonzero

change of the macroscopic electric polarization $\Delta P^{\text{UC}}(t)$. In the first step, we calculate the microscopic polarization $\Delta P(\mathbf{r}, t)$ in the two crystal planes defined in Figs. 5(a) and 5(f), which contain a potassium, a phosphorus, and two oxygen atoms at their equilibrium positions, i.e., for negligible soft-mode elongations. The latter condition is fulfilled at a delay time of 730 fs in the experiments in Ref. [19].

The $\Delta P(\mathbf{r}, t)$ derived from $\Delta\rho(\mathbf{r}, t)$ for a delay time of 730 fs is shown in Figs. 5(b) and 5(g). The changes of microscopic polarization are associated with the transient prolate distortion of electron density on the potassium atom along the c axis, as signaled by a strong positive or negative current density above or below the equilibrium position indicated by a dashed circle. Further significant changes of $\Delta P(\mathbf{r}, t)$ are observed in the P-O bonds and, less pronounced, in the region of the weaker K-O bonds. This behavior bears some similarity to the results for ferroelectric AS (cf. Sec. III), where intraionic charge transfer in the SO_4^{2-} ion occurs along the S-O bonds. In KDP, the four P-O bonds within one phosphate unit display a striking asymmetry: while two bonds are characterized by a positive microscopic polarization [Fig. 5(b)], the other two bonds behave in the opposite fashion [Fig. 5(g)]. It should be noted that the macroscopic polarization $\Delta P^{\text{UC}}(t)$, which is calculated by integrating the microscopic $\Delta P(\mathbf{r}, t)$ over the unit cell, vanishes for the atomic positions in the paraelectric unit cell considered here.

TABLE I. Relation between the IRREPs of space group $I\bar{4}2d$ (KDP in the paraelectric phase) and those of space group $I21d$ ($Fdd2$) (KDP in the ferroelectric phase). The corresponding point groups are mentioned in the second row. The number of corresponding mechanical representations for optical phonons in KDP are mentioned in the first and last rows, respectively.

$I\bar{4}2d$			$I21d$ ($Fdd2$)	
N_{tot}	IRREP of D_{2d} ($\bar{4}2m$)		IRREP of C_{2v} ($mm2$)	N_{tot}
4	A_1	\longleftrightarrow	A_1	10
6	B_2			
5	A_2	\longleftrightarrow	A_2	11
6	B_1		B_1	12
24	E	\longleftrightarrow	B_2	12

Next, we consider the impact of soft-mode excitations of the crystal lattice on the polarization changes. In the first step, the asymmetric nuclear displacements during a coherent soft-mode oscillation need to be determined. Such asymmetric atomic positions determine the asymmetry in the electronic currents creating the microscopic polarization changes $\Delta\mathbf{P}(\mathbf{r}, t)$ and, in turn, a nonvanishing macroscopic polarization change $\Delta\mathbf{P}^{\text{UC}}(t) \neq 0$ in the coherently excited subvolume. To this end, we performed a group theoretical analysis of the optical phonon modes in KDP, which is described in detail in Appendix C. There is an interesting relation between the

IRREPs of the $I\bar{4}2d$ and $I21d$ ($Fdd2$) space groups as shown in Table I. The IRREPs A_1 and B_2 of the paraelectric space group $I\bar{4}2d$ are completely caught up in IRREP A_1 of their ferroelectric counterpart $I21d$ ($Fdd2$). As a direct consequence it is possible to describe the atomic motions occurring during a phase transition from the para- to the ferroelectric state of KDP as coherent phonon motions according to the mechanical representations belonging to IRREPs A_1 and B_2 of space group $I\bar{4}2d$. Tables II and III show the directions of the motion of the P, K, O, and H atoms according to IRREPs A_1 and B_2 . We projected the atomic motions occurring during a phase transition from the para- to the ferroelectric state of KDP onto the 4 mechanical representations belonging to IRREP A_1 and the 6 belonging to B_2 and found that all 10 mechanical representations are relevant for that motion:

$$\begin{aligned} \Delta\mathbf{R}_{I\bar{4}2d}^{\text{para} \rightarrow \text{ferro}} = & -0.000710 \cdot A_1^{O(a)} - 0.001480 \cdot A_1^{O(b)} \\ & + 0.000865 \cdot A_1^{O(c)} - 0.001580 \cdot A_1^H \\ & + 0.014820 \cdot B_2^K - 0.000180 \cdot B_2^{O(a)} \\ & + 0.000530 \cdot B_2^{O(b)} + 0.008825 \cdot B_2^{O(c)} \\ & - 0.026060 \cdot B_2^{H(a)} + 0.009420 \cdot B_2^{H(b)}. \end{aligned} \quad (10)$$

Only atomic motions according to IRREP A_1 of $I\bar{4}2d$ can be directly reconstructed from the differential charge density map $\Delta\rho_{\text{ave}}(\mathbf{r}, t)$ measured in the paraelectric phase, as the intensity changes $\Delta I_{hkl}/I_{hkl}^0$ depend in a linear way (for small amplitudes) on the elongations of A_1 phonon modes. In contrast, $\Delta I_{hkl}/I_{hkl}^0$ depends at lowest order strictly quadratically

TABLE II. The 45 optical phonon modes in paraelectric KDP can be reduced to five different IRREPs according to its space group $I\bar{4}2d$. The table shows the atomic motions of the four mechanical representations belonging to IRREP A_1 possessing the full symmetry of its space group. Wyckoff positions 4a (P atoms) and 4b (K atoms) do not have any mechanical motions according to A_1 . The eigenvectors $A_1^{O(a)}$, $A_1^{O(b)}$, and $A_1^{O(c)}$ of correlated oxygen motions along the relative coordinates Δx , Δy , and Δz are shown for Wyckoff positions 16e and those of A_1^H for correlated hydrogen motions for Wyckoff positions 8d.

Atom	Wyckoff position			O (16e)			H (8d)	
	x	y	z	$A_1^{O(a)}$		$A_1^{O(c)}$	A_1^H	
				Δx	Δy		Δx	Δy
P	0	0	0					
	1/2	0	3/4					
K	0	0	1/2					
	1/2	0	1/4					
O	x	y	z		1	-1		-1
	$-x$	$-y$	z		-1	1		-1
	y	$-x$	$-z$	1			1	1
	$-y$	x	$-z$	-1			-1	1
	$-x + 1/2$	y	$-z + 3/4$		1	1		1
	$x + 1/2$	$-y$	$-z + 3/4$		-1	-1		1
	$-y + 1/2$	$-x$	$z + 3/4$	-1			1	-1
	$y + 1/2$	x	$z + 3/4$	1			-1	-1
	H	x	1/4	1/8				
$-x$		3/4	1/8					1
1/4		$-x$	7/8					
3/4		x	7/8					-1

TABLE III. Atomic motions of the six mechanical representations belonging to IRREP B_2 of space group $I\bar{4}2d$ allowing for a macroscopic polarization along the c direction. Since we consider only optical phonon modes we keep the P atoms at their Wyckoff positions 4a. The eigenvectors B_2^K , $B_2^{O(c)}$, and $B_2^{H(b)}$ describe the collective motions of the K, O, and H atoms along the c direction, respectively. $B_2^{O(a)}$, $B_2^{O(b)}$, and $B_2^{H(a)}$ describe correlated oxygen and hydrogen motions within the ab plane.

Atom	Wyckoff position			K (4b)	O (16e)					H (8d)		
	x	y	z	B_2^K	$B_2^{O(a)}$		$B_2^{O(b)}$		$B_2^{O(c)}$	$B_2^{H(a)}$		$B_2^{H(b)}$
				Δz	Δx	Δy	Δx	Δy	Δz	Δx	Δy	Δz
P	0	0	0									
	1/2	0	3/4									
K	0	0	1/2	1								
	1/2	0	1/4	1								
O	x	y	z			1	-1		1			
	$-x$	$-y$	z			-1	1		1			
	y	$-x$	$-z$		-1			-1	1			
	$-y$	x	$-z$		1			1	1			
	$-x + 1/2$	y	$-z + 3/4$			-1	-1		1			
	$x + 1/2$	$-y$	$-z + 3/4$			1	1		1			
	$-y + 1/2$	$-x$	$z + 3/4$		-1			1	1			
	$y + 1/2$	x	$z + 3/4$		1			-1	1			
H	x	1/4	1/8							-1		1
	$-x$	3/4	1/8							1		1
	1/4	$-x$	7/8							1		1
	3/4	x	7/8							-1		1

on the amplitude of coherent phonon motions belonging to IRREPs A_2 , B_1 , B_2 , and E of $I\bar{4}2d$ [36]. The soft mode in the paraelectric phase of KDP contains relative motions between the K, P, and O atoms along the c axis and definitely belongs to IRREP B_2 . According to IRREP B_2 of $I\bar{4}2d$ the K atom can move along the c axis of the KDP crystal. Since the powder diffraction experiment averages over all manifestations of the structure changes in the unit cell, the initially spherical electron density of the K atom develops as a function of time a cigarlike shape along the c axis with a time-dependent aspect ratio c/a . Such an electron density represents the superposition of two subensembles of unit cells with K atoms having moved into the $+c$ and $-c$ directions. The insensitivity of the sign of the phase of B_2 -mode coherent phonons is another intrinsic property of the probing process via x-ray diffraction from a randomly oriented powder sample. It has nothing to do with the excitation mechanism of coherent phonons belonging to IRREP B_2 of $I\bar{4}2d$, i.e., even for a direct phase-sensitive THz excitation of the soft mode in the paraelectric phase of KDP one cannot derive the sign of the phase of a coherent B_2 phonon from femtosecond powder diffraction data.

For a reconstruction of transient macroscopic polarizations caused by coherent B_2 phonon modes in the paraelectric phase of KDP we proceed as follows: We assume that the entire ensemble of unit cells within the powder sample can be split into two subensembles having the opposite phase of the optically excited coherent B_2 -phonon modes. The relative amplitudes and phases of the motions of various atoms within the unit cell of KDP are taken from the projection of the atomic motions occurring during a phase transition from the para- to the ferroelectric state onto the six mechanical representations belonging to IRREP B_2 of $I\bar{4}2d$ [Eq. (10)]. The amplitude of the soft-mode motion is then derived from the time-dependent

cigarlike shape of the K atoms (cf. Fig. 3 in Ref. [20]). The results of this calculation are presented in Fig. 6(b). This course of action is valid if predominantly strongly polar (i.e., with large LO-TO splittings) low-frequency optical phonon modes are excited as in the femtosecond powder diffraction experiments in Refs. [19] and [20].

The results for the two limiting cases with full B_2 displacements [37] are shown in Figs. 5(c) and 5(h) and Figs. 5(d) and 5(i) as two-dimensional contour maps of the additional changes in the microscopic polarization $\Delta\Delta\mathbf{P}(\mathbf{r}, t) = \Delta\mathbf{P}_{\text{soft mode}}(\mathbf{r}, t) - \Delta\mathbf{P}_{\text{w/o soft mode}}(\mathbf{r}, t)$ relative to $\Delta\mathbf{P}_{\text{w/o soft mode}}(\mathbf{r}, t)$ without soft-mode displacements [Figs. 5(b) and 5(g)]. The additional changes $\Delta\Delta\mathbf{P}(\mathbf{r}, t)$ are predominantly centered on the P-O bonds and are overwhelmingly positive or negative for a positive or negative displacement according to the B_2 mode. This strong imbalance is the microscopic origin of the nonzero macroscopic electric polarization change $\Delta\mathbf{P}^{\text{UC}}(t)$ once an additional displacement of the crystal structure according to the soft mode (IRREP B_2) is introduced. As illustrated in Fig. 5(e), the resulting $\Delta\mathbf{P}^{\text{UC}}(t)$ is linearly proportional to the soft-mode displacement. We note that the macroscopic equilibrium polarization of ferroelectric KNbO_3 as calculated from a Berry phase approach by Resta *et al.* displays a similar linear dependence on lattice elongations [7]. This allows for calculation of the time-dependent macroscopic polarization change during the experimentally observed soft-mode oscillations.

The results are shown in Fig. 6(a) for three cases: (i) no soft-mode displacements (black symbols), (ii) full positive soft-mode displacements (red symbols) [37], and (iii) full negative soft-mode displacement (blue symbols). The soft-mode displacements observed in the experiments [19] are somewhat smaller than the B_2 contribution of the atomic

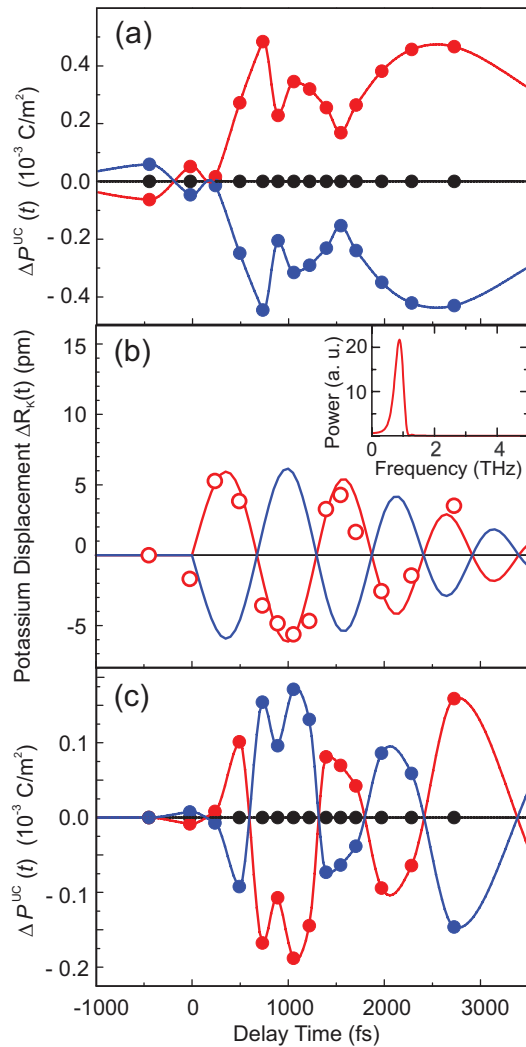


FIG. 6. (a) Time-dependent electronic contributions to the total change of the macroscopic electric polarization $\Delta\mathbf{P}^{\text{UC}}(t)$ as derived from the transient charge density data (symbols, solid lines). Black symbols represent the transient polarization change for the structure with no additional displacement of the ground-state structure, while red and blue symbols represent cases with full positive or negative displacement [37]. (b) Time-dependent displacement of the potassium atom $\Delta R_K(t)$ obtained from the prolate or oblate distortion of the transient electron density $\rho(\mathbf{r}, t)$. (c) Absolute time-dependent polarization change $\Delta\mathbf{P}^{\text{UC}}(t)$ obtained from a calculation of the total change of the macroscopic electric polarization $\Delta\mathbf{P}^{\text{UC}}(t)$ with the time-dependent displacement of the potassium atom $\Delta R_K(t)$ shown in (b), with the color coding of the symbols as in (a). Lines in (a)–(c) are a guide for the eye.

motions occurring during the structural change from the para- to the ferroelectric phase. Their ratio to the maximum values can be derived from the transient electron density maps $\Delta\rho(\mathbf{r}, t)$ by analyzing the distortion of the electron density in the vicinity of the potassium atom from a spherical to a more prolate geometry. The resulting time-dependent displacement of the potassium atom $\Delta R_K(t)$ is plotted in Fig. 6(b) and follows a slowly decaying sinusoidal oscillation, the decay representing the decoherence of the underlying vibrational wave packet. Due to the random orientations of

KDP crystallites in the powder sample, the experiment gives the averaged absolute value of the displacements but not the direction. As a result, either of the two curves shown in Fig. 6(b) can be realized in a particular crystallite. Since the maximum displacement of the potassium atom during the full soft-mode oscillation is known (10.3 pm) [37], $\Delta R_K(t)$ can be used to calibrate the polarization change $\Delta\mathbf{P}^{\text{UC}}(t)$. The result is shown in Fig. 6(c) and gives the total electronic contribution to the macroscopic polarization change during the experimentally observed soft-mode oscillation in KDP.

The results presented in this section establish the first link between transient microscopic electron densities from time-resolved x-ray diffraction experiments and macroscopic electric polarizations of KDP. Complementary experiments with KDP single crystals rather than powder samples will eliminate the orientational averaging over crystallites and, thus, hold potential for generating even more specific insight.

V. CONCLUSION AND OUTLOOK

In conclusion, our results demonstrate the potential of ultrafast x-ray diffraction for unraveling the microscopic mechanisms behind ferroelectricity and for mapping the intrinsically ultrafast dynamics of electric polarizations upon coherent phonon excitation. The fact that time-resolved charge density maps allow for solution of the continuity equation, (7), while at the same time minimizing the kinetic energy [Eq. (9)] of electrons during their quasiadiabatic motion, establishes a natural and most direct link between microscopic charge density changes and microscopic or macroscopic electric polarization changes. This insight will allow for benchmarking of the *ab initio* quantum theory of ferroelectrics and will, thus, be instrumental in understanding and tailoring ferroelectric materials for a wide range of applications.

The tiny asymmetry in the atomic motions during coherent soft-mode oscillations in ferro- or paraelectric crystals strongly influences the electronic currents, the time integral of which represents the transient change of the electronic microscopic polarization (which typically dominates that of the ionic displacements). Thus, future experiments should aim at improving the spatial resolution of the femtosecond x-ray diffraction experiment to determine subtle atomic motions with a higher accuracy. For the experiments on paraelectric crystals, phase-sensitive time-resolved x-ray methods, e.g., measurements of Friedel pairs on single crystals, will provide direct experimental access to the symmetry reduction introduced by coherent soft-mode oscillations.

ACKNOWLEDGMENT

This research was supported by the Deutsche Forschungsgemeinschaft (Grant No. WO 558/13-2).

APPENDIX A: QUASIADIABATIC THEORY FOR ELECTRON MOTIONS ON FINITE TIME SCALES

In his first article on the adiabatic principle in quantum mechanics [11,12] Max Born referred, in the discussion of his equations (18), to the fluid-mechanical formulation of Madelung [38]. The latter concept gives expectation values

of experimental quantities identical to those calculated with the time-dependent Schrödinger equation, (A1):

$$i\hbar \frac{\partial \Psi(\mathbf{r}, t)}{\partial t} = -\frac{\hbar^2}{2m_0} \nabla^2 \Psi(\mathbf{r}, t) + V(\mathbf{r}, t) \Psi(\mathbf{r}, t) \quad (\text{A1})$$

$$\Psi(\mathbf{r}, t) = R(\mathbf{r}, t) \exp[iS(\mathbf{r}, t)], \quad (\text{A2})$$

$$\rho(\mathbf{r}, t) = -e_0 R(\mathbf{r}, t) \cdot R(\mathbf{r}, t), \quad (\text{A3})$$

$$\mathbf{v}(\mathbf{r}, t) = \frac{\hbar}{m_0} \nabla S(\mathbf{r}, t), \quad (\text{A4})$$

$$\frac{d\mathbf{v}(\mathbf{r}, t)}{dt} = \frac{\partial \mathbf{v}(\mathbf{r}, t)}{\partial t} + [\mathbf{v}(\mathbf{r}, t) \cdot \nabla] \mathbf{v}(\mathbf{r}, t), \quad (\text{A5})$$

$$\begin{aligned} m_0 \rho(\mathbf{r}, t) \frac{d\mathbf{v}(\mathbf{r}, t)}{dt} \\ = -\rho(\mathbf{r}, t) \nabla V(\mathbf{r}, t) - \rho(\mathbf{r}, t) \nabla \left[-\frac{\hbar^2}{2m_0} \frac{\nabla^2 \sqrt{|\rho(\mathbf{r}, t)|}}{\sqrt{|\rho(\mathbf{r}, t)|}} \right]. \end{aligned} \quad (\text{A6})$$

The fluid-mechanical approach, which has been used sporadically [39–41], consists of two coupled equations of motion for the electron density $\rho(\mathbf{r}, t)$ [Eq. (A3)] and the electron velocity field $\mathbf{v}(\mathbf{r}, t)$ [Eq. (A4)]. While Eq. (7) is the well-known continuity equation for electronic charge, the last equation (A6) corresponds to an irrotational potential flow in fluid mechanics (Sec. 9 in Ref. [42]). The fluid-mechanical treatment describes the behavior of single electrons [38–41] but can be extended to many-electron systems (cf. discussion around Eq. (18) in Ref. [11]). The equation of motion of the antisymmetric wave function of many indistinguishable electrons can be reduced to equations of motion for single-particle Green functions describing the dynamics of independent quasiparticles [28]. The latter concept corresponds to a single-particle theory with modified potentials due to correlations in the many-body system. The electronic currents in quadiabatic motions flow essentially within the molecular bonds where the electron density is typically quite low. As a result, a single-electron quasiparticle theory according to (A1)–(A6) and (7) is mostly sufficient to describe the quadiabatic polarization dynamics in crystalline matter.

Here, we consider quadiabatic electron motions in systems without any circular electron currents or spin-related effects (i.e., all magnetic effects are considered to be absent). This situation is present in a (ferroelectric) insulator in its electronic ground state or even in electronic excited states if strongly localized (charge-transfer) excitons represent a valid description of the excited state. In such a case the quadiabatic motion occurs essentially on a single vibrational potential surface, far away from any conical intersection. In the fluid-mechanical formulation of quantum mechanics, such a stationary electronic eigenstate has a vanishing velocity field $\mathbf{v}(\mathbf{r}, t) = 0$, i.e., electronic currents are absent and the corresponding kinetic energy according to (9) identically

vanishes. This changes when the nuclei in the system start to move, creating coercively superpositions of electronic states, because electrons can change only their spatiotemporal density $\rho(\mathbf{r}, t)$ by forming moving wave packets which (by definition) are superpositions of several electronic eigenstates of the system. Minimizing the kinetic energy according to (9) ensures that the electronic system stays as close as possible to one electronic eigenstate during the quadiabatic motion. In this sense, our theoretical concept is the first-order extension of the (approximative) wave function in Berry's paper (Eq. (3) in Ref. [10]) describing fully adiabatic electron motion.

APPENDIX B: NUMERICAL PROCEDURE FOR DETERMINING THE MICROSCOPIC CURRENT DENSITY

The microscopic current density $\mathbf{j}(\mathbf{r}, t)$ in Eq. (5) is determined by solving the continuity equation, (7), while at the same time minimizing the kinetic energy [Eq. (9)] of electrons during their quadiabatic motion. To this end we discretized the unit cell into small cubic boxes (voxels) which can exchange electronic charge with their neighboring voxels in the x , y , and z directions. The square interfaces between the boxes define a grid for the microscopic currents j_x , j_y , and j_z . At each instant in time, the given information is the temporal change of the electronic charge $\partial_t Q_v$ in N voxels of the unit cell. Thus, we have in the beginning $3N$ unknown variables for the currents between voxels in the x , y , and z directions. The discretized version of the continuity equation, (7), determines linear relations between a subset of $N - 1$ currents and $N - 1$ charge changes $\partial_t Q_v$ (due to charge conservation the charge change information in one of the voxels is redundant). After inserting these linear relations into the kinetic energy [Eq. (9)] the latter becomes a (bilinear) function of a subset of $2N + 1$ currents with one global minimum. The latter is found simply by solving a system of $2N + 1$ linear equations.

APPENDIX C: GROUP THEORETICAL CONSIDERATIONS AND NORMAL-MODE ANALYSIS

Paraelectric KDP belongs to space group $I\bar{4}2d$ (No. 122 in the ITA), while ferroelectric KDP belongs to its nonisomorphic subgroup $Fdd2$ (No. 43 in the ITA). In both phases the primitive unit cell contains two KH_2PO_4 molecules leading to 45 normal optical phonon modes (at $q = 0$) whose reduction to IRREPs is shown in Tables I and II in Ref. [35]. To elucidate the atomic motions occurring during a paraelectric-to-ferroelectric phase transition in KDP, we adopt the nonconventional setting $I21d$ for the ferroelectric space group $Fdd2$. This allows for a continuous atomic motion within the relative coordinates of the initial paraelectric space group $I\bar{4}2d$, thus avoiding a transformation of the relative coordinates $x' = (x + y)/2$ and $y' = (x - y)$ (cf. caption to Table II in Ref. [35]). Tables II and III show the directions of the motion of the P, K, O, and H atoms according to IRREPs A_1 and B_2 .

- [1] M. E. Lines and A. M. Glass, *Principles and Applications of Ferroelectrics and Related Materials* (Clarendon, Oxford, UK, 1977).
 [2] M. Dawber, K. M. Rabe, and J. F. Scott, *Rev. Mod. Phys.* **77**, 1083 (2005).

- [3] R. W. Boyd, *Nonlinear Optics*, 3rd ed. (Elsevier, Amsterdam, 2008).
 [4] C. Somma, K. Reimann, C. Flytzanis, T. Elsaesser, and M. Woerner, *Phys. Rev. Lett.* **112**, 146602 (2014).
 [5] R. M. Martin, *Phys. Rev. B*, **9**, 1998 (1974).

- [6] R. Resta, *Rev. Mod. Phys.* **66**, 899 (1994).
- [7] R. Resta, M. Posternak, and A. Baldereschi, *Phys. Rev. Lett.* **70**, 1010 (1993).
- [8] D. Vanderbilt and R. D. King-Smith, *Phys. Rev. B* **48**, 4442 (1993).
- [9] R. Resta, *Ferroelectrics* **151**, 49 (1994).
- [10] M. V. Berry, *Proc. R. Soc. Lond. A* **392**, 45 (1984).
- [11] M. Born, *Z. Phys.* **40**, 167 (1926).
- [12] M. Born, *Z. Phys.* **51**, 165 (1928).
- [13] J. C. Slater, *J. Chem. Phys.* **9**, 16 (1941).
- [14] W. Cochran, *Phys. Rev. Lett.* **3**, 412 (1959).
- [15] W. Cochran, *Adv. Phys.* **9**, 387 (1960).
- [16] T. Elsaesser and M. Woerner, *J. Chem. Phys.* **140**, 020901 (2014).
- [17] M. Woerner, F. Zamponi, Z. Ansari, J. Dreyer, B. Freyer, M. Prémont-Schwarz, and T. Elsaesser, *J. Chem. Phys.* **133**, 064509 (2010).
- [18] J. Stingl, F. Zamponi, B. Freyer, M. Woerner, T. Elsaesser, and A. Borgschulte, *Phys. Rev. Lett.* **109**, 147402 (2012).
- [19] F. Zamponi, P. Rothhardt, J. Stingl, M. Woerner, and T. Elsaesser, *Proc. Natl. Acad. Sci. USA* **109**, 5207 (2012).
- [20] F. Zamponi, J. Stingl, M. Woerner, and T. Elsaesser, *Phys. Chem. Chem. Phys.* **14**, 6156 (2012).
- [21] C. Hauf, A.-A. Hernandez Salvador, M. Holtz, M. Woerner, and T. Elsaesser, *Struct. Dyn.* **5**, 024501 (2018).
- [22] R. G. Woolley, *Adv. Chem. Phys.* **33**, 153 (2007).
- [23] N. A. Spaldin, *J. Solid State Chem.* **195**, 2 (2012).
- [24] P. Coppens, *X-ray Charge Densities and Chemical Bonding* (Oxford University Press, Oxford, UK, 1997).
- [25] C. Gatti and P. Macchi (eds.), *Modern Charge-Density Analysis* (Springer, Heidelberg, 2012).
- [26] F. Zamponi, Z. Ansari, M. Woerner, and T. Elsaesser, *Opt. Express* **18**, 947 (2010).
- [27] S. Smaalen, L. Palatinus, and M. Schneider, *Acta Crystallogr. A* **59**, 459 (2003).
- [28] M. Woerner, M. Holtz, V. Juvé, T. Elsaesser, and A. Borgschulte, *Faraday Disc.* **171**, 373 (2014).
- [29] S. Ahmed, A. Shamah, K. Kamel, and Y. Badr, *Phys. Status Solidi (a)* **99**, 131 (1987).
- [30] Crystallographic data (excluding structure factors) of the time-independent diffraction experiment on AS have been deposited with the Cambridge Crystallographic Data Centre as supplementary publication no. CCDC 1855567.
- [31] R. J. Nelmes, Z. Tun, and W. F. Kuhs, *Ferroelectrics* **71**, 125 (1987).
- [32] G. F. Reiter, J. Mayers, and P. Platzman, *Phys. Rev. Lett.* **89**, 135505 (2002).
- [33] Q. Zhang, F. Chen, N. Kioussis, S. G. Demos, and H. B. Radousky, *Phys. Rev. B* **65**, 024108 (2001).
- [34] F. Brehat, B. Wyncke, and A. Hadni, *Phys. Status Solidi (b)* **107**, 723 (1981).
- [35] P. Simon, F. Gervais, and E. Courtens, *Phys. Rev. B* **37**, 1969 (1988).
- [36] Although this behavior is expected for symmetry reasons we checked it numerically with artificial atomic displacements within the spherical independent atom model, i.e., without any electronic charge transfer.
- [37] We denote a full B_2 displacement with the situation that the nuclei are displaced by the B_2 contribution [cf. Eq. (10)] of the atomic motions occurring during the paraelectric-to-ferroelectric phase transition.
- [38] E. Madelung, *Z. Phys.* **40**, 322 (1926).
- [39] L. Janossy, *Z. Phys.* **169**, 79 (1962).
- [40] H. E. Wilhelm, *Phys. Rev. D* **1**, 2278 (1970).
- [41] C. L. Loppreore and R. E. Wyatt, *Phys. Rev. Lett.* **82**, 5190 (1999).
- [42] L. D. Landau and E. M. Lifshitz, *Fluid Mechanics*, 2nd ed. Course of Theoretical Physics, Vol. 6 (Elsevier, Amsterdam, 1987).